

Energy dispersion in radiation pressure accelerated ion beams

**M Grech^{1,6}, S Skupin^{1,2}, A Diaw³, T Schlegel⁴
and V T Tikhonchuk⁵**

¹ Max-Planck-Institute for the Physics of Complex Systems, D-01187 Dresden, Germany

² Friedrich Schiller University, Institute of Condensed Matter Theory and Solid State Physics, D-07743 Jena, Germany

³ Centre de Physique Théorique, Ecole Polytechnique, F-91128 Palaiseau, France

⁴ Helmholtz Institute Jena, D-07743 Jena, Germany

⁵ Centre Lasers Intenses et Applications, F-33405 Talence, France

E-mail: mickael.grech@gmail.com

New Journal of Physics **13** (2011) 123003 (20pp)


Received 24 May 2011

Published 1 December 2011

Online at <http://www.njp.org/>

doi:10.1088/1367-2630/13/12/123003

Abstract. We address the problem of energy dispersion of radiation pressure accelerated (RPA) ion beams emerging from a thin target. Two different acceleration regimes, namely phase-stable acceleration and multistage acceleration, are considered by means of analytical modeling and one-dimensional particle-in-cell simulations. Our investigations offer a deeper understanding of RPA and allow us to derive some guidelines for generating monoenergetic ion beams.

 Online supplementary data available from stacks.iop.org/NJP/13/123003/mmedia

⁶ Author to whom any correspondence should be addressed.

Contents

1. Introduction	2
2. Basic modeling	3
2.1. Macroscopic approach: the light-sail model	3
2.2. Scaling laws for the ion energy	4
3. Two radiation pressure acceleration (RPA) regimes	5
3.1. Phase-stable acceleration of thin targets	5
3.2. Multistage RPA of thicker targets	7
4. Numerical simulations	9
4.1. Optimal target thickness	10
4.2. Ion acceleration in the phase-stable regime	10
4.3. Ion acceleration in the multistage regime	14
5. Conclusion	18
Acknowledgments	19
References	19

1. Introduction

Interaction of ultra-intense laser pulses with thin foils offers interesting possibilities to generate energetic charged particles. The so-called radiation pressure acceleration (RPA) of ion bunches has recently attracted much interest as it may provide an efficient way of generating intense quasi-monoenergetic ion beams. In contrast to target normal sheath acceleration (TNSA) [1, 2], where ions are accelerated from the target rear surface (the front surface being the one irradiated by the laser pulse) in the electrostatic field built up by the laser-created hot electrons, RPA of ion beams relies on efficient momentum transfer from laser photons to ions in a thin dense target, which reflects the incident laser pulse. Therefore, RPA may provide a very efficient way to accelerate quasi-neutral ion–electron bunches up to potentially relativistic velocities while keeping the energy dispersion small.

The idea of accelerating (macroscopic) objects by laser radiation pressure was initially discussed by Marx [3] as a possible path toward interstellar space travel. Its application to efficient ion acceleration was first proposed in [4], where the authors show that, in order to observe efficient RPA with linearly polarized light, ultra-high laser intensities ($I_L \gtrsim 10^{23} \text{ W cm}^{-2}$) are required. For lower intensities, indeed, strong laser-induced electron heating makes target expansion the dominant acceleration mechanism. In 2005, Macchi *et al* [5] demonstrated that using circularly polarized (CP) laser light strongly reduces electron heating, thus allowing RPA to operate efficiently at lower intensities. After that, different teams have discussed independently the possibility of creating quasi-monoenergetic ion beams by irradiating a thin target with an intense CP laser pulse [6–9]. Many studies have followed, some proposing and/or revisiting different acceleration models or discussing the optimal laser–target parameters through one-dimensional (1D) and 2D particle-in-cell (PIC) simulations [10–13]. Multi-dimensional effects on the stability of the accelerated foil and their potential capability to improve RPA have also been discussed [14–16]. Finally, the first experimental confirmation of RPA was claimed recently [17].

While the basic mechanisms of RPA are now well understood, the control of the energy dispersion in RPA ion beams has not been fully addressed. This paper is intended to provide the reader with guidelines on how to achieve this control. To do so, we first recall the basic modeling of RPA of a thin foil and provide scaling laws concerning the maximum ion energy that can be reached as a function of laser intensity or power (section 2). Beyond this simple (macroscopic) modeling, we discuss the details of RPA of a thin foil as following from two complementary processes. For the thinnest foils, electrons are piled up at the target rear side by the strong radiation pressure. Ion acceleration then proceeds in the so-called phase-stable way [9], where ions are continuously accelerated in the resulting charge-separation field. In contrast, thick enough targets undergo multiple successive hole-boring stages so that ion acceleration occurs as a discontinuous, multi-step process [6, 7]. In section 3, we propose some refined models for both acceleration processes and extract the main requirements for controlling the resulting ion energy dispersion. These analytical findings are compared to numerical PIC simulations in section 4. Finally, we present our conclusions in section 5.

2. Basic modeling

In this paper, all quantities are normalized to laser- and electron-related units. Times and distances are normalized to the incident laser frequency ω_L and wave number $k_L = \omega_L/c$, respectively, and velocities are normalized to the light velocity c . Electric charges and masses are normalized to the electron charge e and mass m_e , respectively. Densities are normalized to the critical density at the considered laser wavelength $\lambda_L = 2\pi/k_L$: $n_c = \epsilon_0 m_e \omega_L^2/e^2$, where ϵ_0 is the permittivity of free space. Electric fields are normalized to the Compton field $E_C = m_e c \omega_L/e$. Furthermore, we consider a CP laser pulse and introduce the incident laser pulse vector potential:

$$\mathbf{A}_L(t, x) = \frac{a_L(t)}{\sqrt{2}} [\cos(t - x) \hat{\mathbf{y}} + \sin(t - x) \hat{\mathbf{z}}], \quad (1)$$

where $\hat{\mathbf{y}}$ and $\hat{\mathbf{z}}$ denote the unit vectors pointing in the two directions transverse to the laser propagation direction $\hat{\mathbf{x}}$.

2.1. Macroscopic approach: the light-sail model

A straightforward and elegant way of deriving the energy ions gain during the acceleration of a thin target by laser radiation pressure is to consider the accelerated layer as a quasi-neutral light sail reflecting the incident laser pulse [4]. Acceleration then follows from momentum transfer from the laser photons to the ions. Assuming that all ions in the target have the same velocity $v_i^{(1)}$ in the laboratory frame, the equation of motion for the target is obtained by equating the photon momentum flux to the ion momentum flux, which follows from the target acceleration $(n_{i0} d_0) dp_i^{(1)}/dt$, where $p_i^{(1)}$ is the ion momentum in units of $m_e c$, n_{i0} is the initial target ion density and d_0 its thickness. For arbitrary target velocities, two effects—the reduction of the photon flux on the target and the Doppler shift lowering of the photon momenta in the target frame—must be taken into account. Considering total reflection of the laser pulse in the target frame, one obtains

$$(n_{i0} d_0) \frac{d}{dt} p_i^{(1)} = a_L^2 [t - x_i(t)] \gamma_i^2 (1 - v_i^{(1)})^2, \quad (2)$$

where $a_L^2(t)$ is the normalized laser intensity, $x_i(t)$ is the time-dependent position of the target moving with the velocity $v_i^{(1)}$, and $\gamma_i = (1 - v_i^{(1)2})^{-1/2}$ is the associated Lorentz factor. The solution of equation (2) has been derived, e.g. in [8], for a laser pulse with an idealized step-like temporal profile ($a_L^2(t) = a_0^2$ for $t > 0$ and $a_L^2(t) = 0$ otherwise), with the maximum laser field amplitude a_0 :

$$p_i^{(1)}(t) = m_i [\sinh\phi - (4 \sinh\phi)^{-1}], \quad (3)$$

where $\phi = (1/3) \sinh^{-1}(3 a_0^2 t / (n_{i0} m_i d_0) + 2)$ and m_i is the ion mass.

At this point, we stress that, in the derivation of equation (2), (i) the electron momenta have been neglected and (ii) the target is assumed to be thin enough to be accelerated as a whole, quasi-neutral bunch, but thick enough to support the laser radiation pressure. Both assumptions are discussed in more detail in section 3.

2.2. Scaling laws for the ion energy

Let us now derive some scaling laws for the ion energy $\mathcal{E}_i = (\gamma_i - 1) m_i$ (in units of $m_e c^2$). First, equation (3) can be simplified in the limit of non-relativistic ions ($p_i^{(1)} \ll 1$), leading to $p_i^{(1)}(t) \sim a_0^2 t / (n_{i0} d_0)$ and ion energies:

$$\mathcal{E}_i \sim \frac{m_i}{2} \left(\frac{a_0^2 t}{m_i n_{i0} d_0} \right)^2. \quad (4)$$

This result suggests that the ion energy scales with the square of the laser intensity $I_L = a_0^2$ (in units of $c^3 m_e n_c / 2$) and more precisely with the square of the laser fluence $\phi_L = \int_0^t a_L^2(t) dt$ (in units of $c^3 m_e n_c / (2 \omega_L)$). However, this scaling applies only for sufficiently short laser pulses. Indeed, if the laser pulse is long enough for the target to travel over a distance larger than the laser Rayleigh length $L_R \sim w_L^2$ (w_L is the transverse size of the laser focal spot), diffraction of the laser pulse must be accounted for⁷. It sets in after a time $t \sim \sqrt{2 m_i n_{i0} d_0} w_L / a_0$, so that the final ion energy is limited to $\mathcal{E}_i \sim a_0^2 w_L^2 / (n_{i0} d_0)$. For a sufficiently long laser pulse, the ion energy thus scales (only) linearly with the laser intensity. More precisely, one can introduce the normalized laser power onto the target, $P_L \sim a_0^2 w_L^2$ (in units of $m_e n_c c^3 / (2 k_L^2)$), and we obtain that the final ion energy scales linearly with the laser power.

Considering characteristic diamond-like carbon (DLC) targets ($m_i = 12 \times 1836$, $n_{i0} = 60$ at $\lambda_L = 1 \mu\text{m}$) with thickness $d_0 / \lambda_L = 10^{-2}$ ([18] and references therein) irradiated by a tightly focused laser pulse ($w_L / \lambda_L = 5$), we find that relativistic carbon ions may be obtained using a 100 TW (1 PW) laser with pulse duration ~ 200 fs (~ 20 fs). Hence, relativistic ion production may be possible on already (or soon to be) available laser facilities.

Finally, equation (3) can also be simplified in the limit of ultrarelativistic ions $p_i^{(1)} \gg 1$:

$$\mathcal{E}_i \sim p_i^{(1)} \sim \frac{m_i}{2} \left(\frac{6 a_0^2 t}{m_i n_{i0} d_0} \right)^{1/3}. \quad (5)$$

The ion energy thus increases as $t^{1/3}$. This characteristic evolution was first reported in the original paper by Esirkepov *et al* [4]. In the ultra-relativistic regime, $v_i^{(1)} \sim 1$, and diffraction

⁷ Our estimates of the effect of laser beam diffraction are quite rough as we aim at deriving simple scaling laws for the ion energy. As discussed in [16], the target deformation during the acceleration process may actually prevent the laser beam diffraction and thus allows for enhanced ion energies.

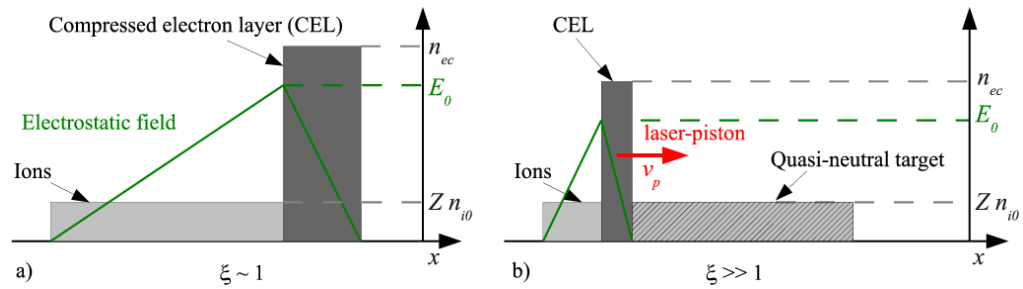


Figure 1. Schematic picture of RPA once the balance between electrostatic and radiation pressures is reached. (a) In the phase-stable regime ($\xi \sim 1$): the target rear side is continuously accelerated. (b) In the multistage regime ($\xi \gg 1$): the laser acts as a piston and ion acceleration occurs sequentially.

sets in after a time $t \sim w_L^2$. The final ion energy then scales as the power $1/3$ of both the laser intensity and power. This is mainly because of photon red-shifting and the reduced photon flux onto the target due to its relativistic recoil.

3. Two radiation pressure acceleration (RPA) regimes

A deeper insight into RPA of thin targets requires us to investigate more closely the structure of the accelerated target. When exposed to an intense laser pulse, the target electrons are pushed forward into the target by the laser ponderomotive force, thus forming a compressed electron layer (CEL) at the laser front. The formation of this layer occurs in a very short time as it involves only electron motion. Its characteristic position l_c before ion motion sets in can be easily derived from equating the electrostatic pressure $(Z n_{i0} l_c)^2/2$ to the radiation pressure a_0^2 on the CEL. Obviously, maintaining the target integrity requires l_c to be smaller than the target thickness d_0 . It is thus quite natural to introduce the normalized parameter $\xi = Z n_{i0} d_0 / (\sqrt{2} a_0)$. For $\xi < 1$, the radiation pressure is so strong that it cannot be balanced by the electrostatic pressure inside the target. All electrons are expelled from the target, which then undergoes Coulomb explosion. This regime of interaction has been studied in [20–22], where the authors have considered its applications to both electron and ion acceleration. It is however not suitable for efficient RPA of thin foils, which requires $\xi \geq 1$.

In what follows, we analyze two regimes of thin foil RPA for parameter values $\xi \sim 1$ or $\xi \gg 1$.

3.1. Phase-stable acceleration of thin targets

In the regime where $\xi \sim 1$, the radiation pressure is strong enough to push all electrons at the target rear side. A large electrostatic field is built up in the whole target and ions are continuously accelerated (see figure 1(a)) as they follow the compressed electron bunch. This regime that was first discussed by Yan *et al* [9] was named phase-stable acceleration by analogy with conventional radiofrequency linear accelerator techniques to keep particles in synchronization with the accelerating field. It is also referred to as self-organized double-layer acceleration [11] or coherent acceleration of ions by laser [19].

For the sake of simplicity, one assumes that the electron density in the CEL is constant and homogeneous: $n_{ec} \sim Z n_{i0} d_0/l_e$, where $l_e < d_0$ is the CEL thickness. At this point, we stress that simple considerations on the balance between electrostatic and radiation pressures do not allow us to derive this thickness l_e . For $\xi = 1$, l_e would indeed shrink to 0, which is prevented by the electron pressure that is not included in our model.

As ions initially located outside the CEL are accelerated in an electrostatic field, which increases linearly in space, they are, *a priori*, not of interest for efficient generation of quasi-monoenergetic ion bunches. We should thus focus our attention on the ions located in the CEL, which undergo acceleration in the monotonically decreasing field:

$$E_x(t, x) = E_0(t) \frac{d(t) - x}{l_e}, \quad (6)$$

where $d(t)$ is the position of the target rear side at time t , and the maximum electrostatic field $E_0(t)$ can be derived from the equilibrium condition of the CEL (in the frame moving with the target rear side):

$$\frac{1}{2} (Z n_{i0} l_e) E_0(t) = a_0^2 \gamma_i^2 (1 - v_i^{(1)})^2, \quad (7)$$

where $v_i^{(1)}$ is the velocity (in the laboratory frame) of the CEL, i.e. of ions accelerated in a phase-stable way, and $\gamma_i = (1 - v_i^{(1)2})^{-1/2}$ is the associated Lorentz factor. From this, we obtain

$$E_0(t) = \sqrt{2} a_0 \gamma_i^2 (1 - v_i^{(1)})^2. \quad (8)$$

Note that in this regime, where electrons are piled up at the rear side of the target, the accelerating field $E_0(t)$ does not depend on the CEL thickness l_e . A similar feature was discussed in [12].

The governing equation for the mean ion momentum can be easily derived by considering that, in the phase-stable regime, ions are accelerated, on the average, by an electrostatic field $E_0(t)/2$. We obtain

$$\frac{d}{dt} p_i^{(1)} = \frac{Z a_0}{\sqrt{2}} \gamma_i^2 (1 - v_i^{(1)})^2, \quad (9)$$

which is nothing but equation (2) derived in the macroscopic model for $\xi \sim 1$.

As for the ion motion around the mean velocity $v_i^{(1)}$, it can be described as in [9]. Denoting $\chi_i(t)$ the position of an arbitrary ion in the CEL with respect to the center of the CEL and considering that all ions move with a velocity close to the mean velocity $v_i^{(1)}$, we obtain

$$\frac{d^2}{dt^2} \chi_i = -\frac{Z E_0(t)}{m_i l_e \gamma_i^3} \chi_i. \quad (10)$$

Therefore, if both $E_0(t)$ and γ_i vary slowly on a time scale Ω^{-1} , where $\Omega^2 = Z E_0(t)/(m_i l_e \gamma_i^3)$, the ions in the CEL have a harmonic motion around the mean velocity. From this, one can infer the dispersion in ion velocities of the accelerated bunch $\Delta v_i \sim l_e \Omega$ in the frame moving with the CEL. Correspondingly, the relative energy dispersion for non-relativistic ions scales as

$$\frac{\Delta \mathcal{E}_i}{\mathcal{E}_i} \propto \left(\frac{Z l_e a_0}{\mathcal{E}_i} \right)^{1/2}. \quad (11)$$

This scaling with $\mathcal{E}_i^{-1/2}$ ensures, with the small CEL thickness $l_e \ll 1$, the quasi-monoenergetic feature of the accelerated ion beam. In the ultrarelativistic regime, one would obtain

$\Delta\mathcal{E}_i/\mathcal{E}_i \propto \mathcal{E}_i^{-5/2}$. However, and as will be shown in numerical simulations (section 4.2), the reduction of radiation pressure in the target frame associated with its relativistic recoil does not allow for this acceleration regime to be maintained at ultrarelativistic velocities. Instead, acceleration will more and more evolve like the multistage process discussed in section 3.2.

Phase-stable acceleration of the thin target thus opens an interesting path toward the creation of energetic quasi-monochromatic ion beams. Nevertheless, there is one restriction that was not mentioned in the original paper by Yan *et al* [9] that we want to address now. In this specific regime of laser–target interaction, the electron bunch is compressed at the target rear side. A large energy can thus be stored in the electrostatic field. Once the laser pulse is turned off, this energy is transferred back to the electrons, which start to quiver around the target, thus inducing its adiabatic expansion and in turn widening the ion energy spectrum.

To estimate the importance of this effect, we derive the energy stored in the electrostatic field (see also [12]). Neglecting the contribution of the CEL due to its small thickness and considering that the electrostatic field varies linearly, $E_x(x) = E_0(t)x/d(t)$ for $0 < x < d(t)$, the energy stored in the electrostatic field reads

$$\mathcal{E}_{\text{es}}(t) \sim \int_0^{d(t)} \frac{E_x^2(x)}{2} dx = \frac{a_0^2}{3} \gamma_i^4 \left(1 - v_i^{(1)}\right)^4 d(t). \quad (12)$$

For non-relativistic ion velocities this quantity simplifies to $\mathcal{E}_{\text{es}}(t) \sim n_{i0} d_0 \mathcal{E}_i(t)/3$, suggesting that the energy stored in the electrostatic field is of the same order as the total ion kinetic energy. For such ion velocities, one should therefore expect a broadening of the ion energy distribution once the laser is turned off. For ultrarelativistic velocities however, \mathcal{E}_{es} is found to remain much smaller than the total kinetic ion energy, and the effect of adiabatic expansion on energy dispersion is negligible.

These theoretical predictions are compared to numerical simulations in section 4.2.

3.2. Multistage RPA of thicker targets

For $\xi \gg 1$, the radiation pressure can only push electrons at a distance $l_c \ll d_0$ inside the target so that the resulting charge separation field remains confined to a region much thinner than the target itself (see figure 1(b)). As we will see, this field structure actually acts as a piston reflecting ions as it propagates deeper into the target. Ion acceleration in this regime can then be described as a multistage process [6, 7], where the target undergoes successive hole-boring (HB) processes.

For the sake of clarity, we first present the multistage process in the case of non-relativistic ion velocities. Then we generalize the procedure to the relativistic case.

3.2.1. Non-relativistic ion velocities. In a first stage, ion acceleration follows from the laser-driven HB of the immobile target. The laser acts on the target ions as a piston, moving deeper into the target with the velocity v_{p0} and reflecting an increasing number of ions [23, 24]. The piston velocity can be derived easily by considering the balance of radiation and electrostatic pressure in the frame comoving with the piston. If the laser field amplitude a_0 and the target density n_{i0} are constant, v_{p0} will not change in time. For non-relativistic ion velocities, we obtain $v_{p0} = a_0/\sqrt{2m_i n_{i0}}$. During this stage, the ion velocity in the laboratory frame ranges between $v_i^{(1)} = 0$ (corresponding to ions having not been picked up by the laser piston) and $v_{i,1}^{(1)} = 2v_{p0}$ (corresponding to ions that have been reflected once by the laser piston). Index 1 in the ion velocity denotes the first acceleration stage. This first stage lasts up to the time $\tau_0 = d_0/v_{p0}$ when

the piston reaches the initial position of the back of the target. Ideally, at the end of this stage, all ions of the target have been accelerated to the velocity $v_{i,1}^{(1)} = 2 v_{p0}$ in the laboratory frame and the whole target has been accelerated as a quasi-neutral bunch. At this point, we restrict ourselves to thin targets with thickness $d_0 \ll v_{p0} t_p$ (with t_p being the laser pulse duration), a necessary condition for the multistage process of RPA. Targets with larger thickness will only undergo HB.

To describe the second acceleration stage, i.e. for times $t > \tau_0$, we consider that the whole target is moving with the velocity $v_t^{(1)} = v_{i,1}^{(1)} = 2 v_{p0}$ in the laboratory frame. Then, in the frame moving with the target, ion acceleration proceeds in a way similar to laser-driven HB. During this stage, ion velocities range between 0 and $2 v_{p0}$ in the target frame, which transforms to $v_t^{(1)} = 2 v_{p0}$ and $v_{i,2}^{(1)} = v_t^{(1)} + 2 v_{p0} = 4 v_{p0}$ in the laboratory frame.

Then, if $t_p > 2 \tau_0$, a third acceleration stage starts during which the ion velocity in the laboratory frame ranges between $4 v_{p0}$ and $6 v_{p0}$. For a sufficiently long laser pulse, this multistage process goes on so that at the j th stage, the ion velocity ranges between $v_{i,j-1}^{(1)} = 2(j-1) v_{p0}$ and $v_{i,j}^{(1)} = 2j v_{p0}$. Correspondingly, the ion energy ranges between $2(j-1)^2 m_i v_{p0}^2$ and $2j^2 m_i v_{p0}^2$. Generation of quasi-monoenergetic ion bunches thus requires the acceleration process to occur over many steps, i.e. over a time $t \gg \tau_0$. If this condition is satisfied, the ion mean energy and energy dispersion at a time $t \sim j \tau_0$ ($j \gg 1$) read

$$\mathcal{E}_i(t) = 2 m_i v_{p0}^2 (t/\tau_0)^2, \quad (13)$$

$$\Delta \mathcal{E}_i(t) = (2 \tau_0/t) \mathcal{E}_i(t). \quad (14)$$

The first equation corresponds to the ion energy evolution expressed by equation (4), which was obtained using the macroscopic model in section 2.1 in the limit of non-relativistic ion velocities. The second relation gives information about the energy dispersion of the ion bunch.

3.2.2. Iterative procedure for relativistic ion velocities. To extend the multistage model to higher ion velocities, relativistic effects such as the radiation pressure diminution on the target and dilation of the characteristic stage duration due to the target relativistic recoil have to be accounted for.

The initial stage of ion acceleration is once more similar to the laser-driven HB of the immobile target. Accounting for relativistic effects, the piston velocity is $v_p = v_{p0}/(1 + v_{p0})$. During this stage, ion velocities thus range between 0 (not yet reflected ions) and $v_{i,1}^{(1)} = 2 v_p/(1 + v_p^2)$ (reflected ions). Correspondingly, we obtain the minimum and maximum ion energies during the first stage: $\mathcal{E}_{i,1}^{\min} = 0$ and $\mathcal{E}_{i,1}^{\max} = (\gamma_i - 1) m_i$, where $\gamma_i = (1 - v_i^{(1)2})^{-1/2}$. This stage ends when the piston reaches the initial position of the target rear side, i.e. after a time $\tau_s^{(1)} = d_0/v_p$. In contrast to the classical limit, however, ions do not reach exactly twice the piston velocity. As a consequence, the target thickness and consequently the ion density have changed. At the end of this first acceleration stage, we have $d_1 = v_{i,\max}^{(1)} \tau_s^{(1)} - d_0$ and $n_{i,1} = n_{i0} d_0/d_1$.

Let us now consider the j th stage of the acceleration process ($j > 1$). The target velocity (in the laboratory frame) is the velocity that ions have reached at the former $j-1$ stage: $v_t^{(1)} = v_{i,j-1}^{(1)}$. In the frame moving with the target, the laser radiation pressure is therefore reduced by the factor $\gamma_t^2 (1 - v_t^{(1)2})^2$ (where $\gamma_t = (1 - v_t^{(1)2})^{-1/2}$). The piston velocity in the target frame thus reads $v_p^{(t)} = v_p'/(1 + v_p')$, where $v_p' = v_{p0} (n_{i0}/n_{i,j-1})^{-1/2} \gamma_t (1 - v_t^{(1)})$. It follows that the reflected ions have a velocity $v_i^{(t)} = 2 v_p^{(t)}/(1 + v_p^{(t)2})$ in the frame moving with the target,

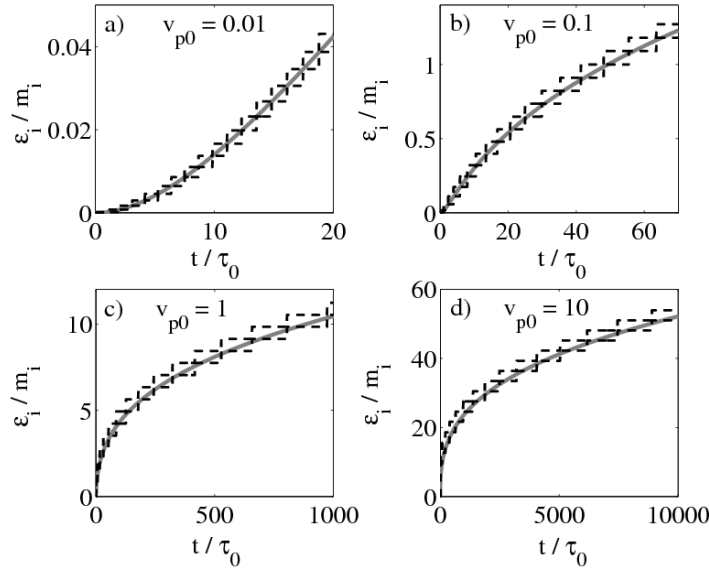


Figure 2. Ion maximum and minimum energies predicted by the multistage model (dashed curves) and comparison to predictions from the macroscopic model (gray solid curves) for (a) $v_{p0} = 0.01$, (b) $v_{p0} = 0.1$, (c) $v_{p0} = 1$ and (d) $v_{p0} = 10$.

which transforms in $v_{i,j}^{(l)} = (v_i^{(t)} + v_t^{(l)}) / (1 + v_i^{(t)} v_t^{(l)})$ in the laboratory frame. The duration of the stage in the target frame is easily computed as $\tau_s^{(t)} = d_{j-1} / v_p^{(t)}$, while one has to account for time dilation in the laboratory frame $\tau_s^{(l)} = \gamma_t \tau_s^{(t)}$. As for the target thickness and density at the end of the stage, they have to be recalculated in the target frame as $d_j = v_i^{(t)} \tau_s^{(t)} - d_{j-1}$ and $n_{i,j} = n_{i0} d_0 / d_j$.

Following this procedure, we can compute the temporal evolution of the minimum and maximum ion energies for arbitrary values of the parameters v_{p0} and d_0 . The comparison of this multistage model with the macroscopic model of section 2.1 is given in figure 2 for several values of v_{p0} . Predictions from the multistage model match perfectly with the results from section 2.1 for $v_{p0} = 0.01$, where the characteristic ion energy evolution $\propto (t/\tau_0)^2$ is recovered (figure 2(a)). For higher values of v_{p0} (figures 2(b)–(d)), good agreement is still found between the two models. A small discrepancy can, however, be observed in the ion mean energy⁸, but it remains small compared to the predicted energy dispersion. It must also be noted that the characteristic duration of an acceleration stage, for relativistic ion velocities, can be strongly dilated in the laboratory frame, which has an important effect on energy dispersion. These analytical predictions are compared to numerical simulations in section 4.3.

4. Numerical simulations

Numerical simulations of RPA of thin targets have been performed using the PIC code PICLS [27]. In order to make a direct comparison with our analytical model, only 1D in space

⁸ Our multistage model predicts a slightly higher ion energy than the macroscopic model. This is because, in our multistage model, we have a step-like decrease of the radiation pressure onto the target, while radiation pressure is continuously decreasing in the macroscopic model.

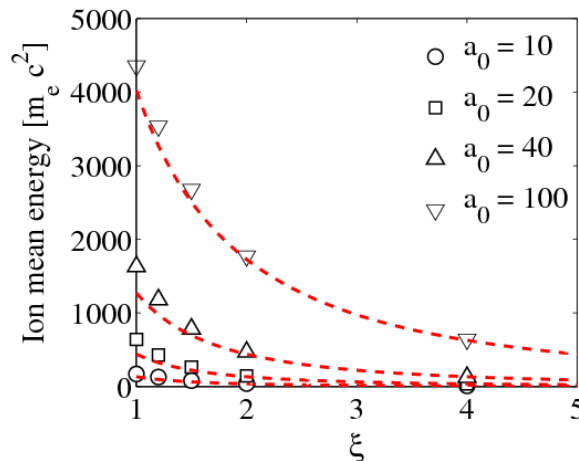


Figure 3. Dependence of the ion mean energy on the normalized parameter ξ (proportional to the target thickness) $\simeq 10 \tau_L$ after the beginning of the interaction. The carbon target has density $Z n_{i0} = 150$ and the laser field amplitude is $a_0 = 10$ (\circ), $a_0 = 20$ (\square) and $a_0 = 40$ (\triangle). Red dashed lines correspond to predictions from the macroscopic (light-sail) model (solutions of equation (2)).

and 3D in velocity (1D3V) simulations are presented. This choice is also justified, as it has been shown that a quasi-1D geometry is required to avoid strong electron heating and partial transparency of the foil, which may prevent quasi-monoenergetic ion beam generation [7]. Our study thus provides us with necessary, albeit not sufficient, conditions for creating monoenergetic ion beams.

In our simulations, a CP laser pulse is focused at normal incidence on a thin, fully ionized, carbon target with density $n_{i0} = 25$ and $Z = 6$. The target is located at a distance $2 \lambda_L$ from the left boundary of the simulation box (the laser propagates from left to right). Both the incident laser field amplitude and the target thickness are varied to explore different regimes of RPA of thin foils.

4.1. Optimal target thickness

Figure 3 shows the ion mean energy at an instant $t \simeq 10 \tau_L$ after the beginning of the interaction for $\xi \geq 1$. In the case $\xi < 1$, the simulations indeed confirm that all electrons are removed from the target due to the strong radiation pressure, leading to the Coulomb explosion of the non-neutralized ion layer. For $\xi \geq 1$, one observes that the ion mean energy increases as the target thickness decreases: the lighter the target, the higher ion energy one can reach. Such a result was already discussed in [10, 12] with the conclusion that the regime, $\xi \sim 1$, is the optimum case for high-energy ion generation.

4.2. Ion acceleration in the phase-stable regime

Let us have a more detailed look at ion acceleration in the phase-stable regime $\xi \sim 1$. Figure 4 presents the time-resolved energy spectra obtained in simulations for different

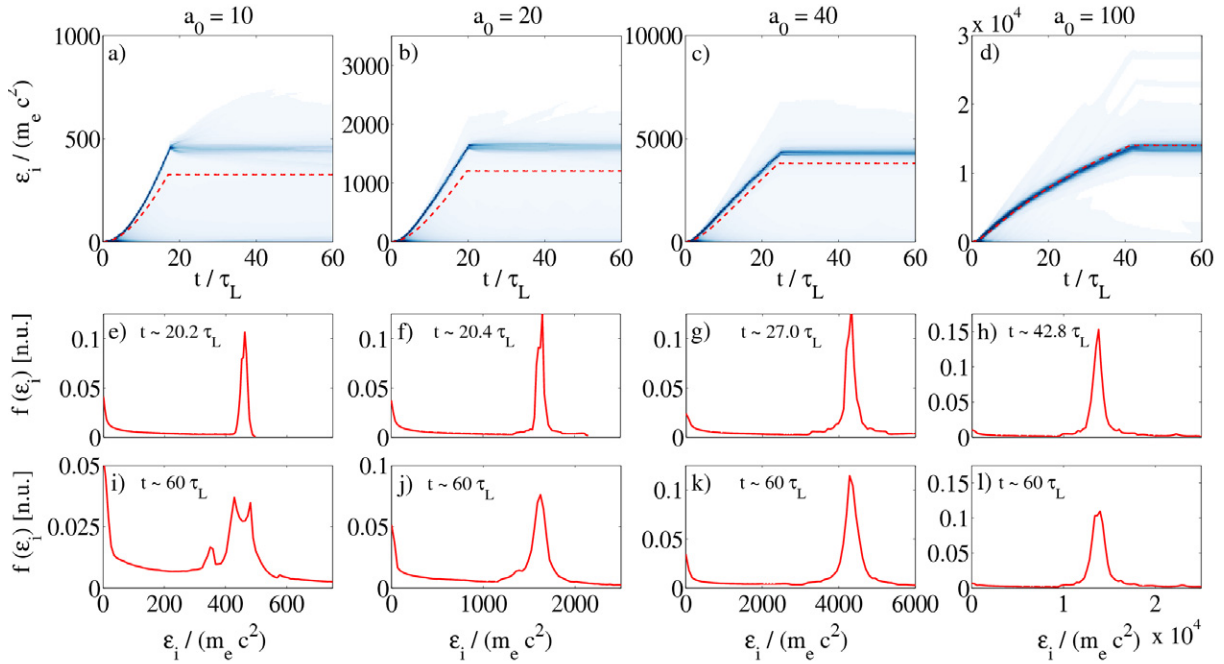


Figure 4. Phase-stable acceleration ($\xi = 1$). (a–d) Time-resolved ion energy spectra. (e–h) Snapshot of the energy spectrum at the end of the laser–target interaction. (i–l) Snapshot of the energy spectrum at the end of the simulation. The laser field amplitude is (a, e, i) $a_0 = 10$, (b, f, j) $a_0 = 20$, (c, g, k) $a_0 = 40$ and (d, h, l) $a_0 = 100$. Red dashed lines show theoretical predictions from the macroscopic model.

incident laser field amplitudes $a_0 = 10$ – 100 and $\xi \sim 1$ (the target thickness is adjusted for each laser amplitude). Theoretical predictions for the ion mean energy from the macroscopic model (section 2.1) are superimposed on to the numerical results. Rather good agreement is found between theory and simulation. However, while for $a_0 = 100$ the ion mean energy evolves exactly as predicted by the macroscopic model, numerical simulations at lower field amplitudes ($a_0 = 10$ – 20) show higher ion energies than estimated analytically. The reason for this discrepancy can be found in figure 5 and the corresponding movies, where details of the temporal evolution of the target structure during the acceleration process are presented for $a_0 = 10$ and $a_0 = 100$. For the lower laser field amplitude, $a_0 = 10$, the CEL is not totally opaque to the laser field, which is partly transmitted (the foil transmittance is here $T \simeq 20\%$). The ponderomotive force on the target rear side is thus non-zero and some electrons can escape from the target into the vacuum behind. This widens the electrostatic field distribution and increases its average value at the target rear side, thus leading to the observed increase of ion energy. In contrast, for $a_0 = 100$, the target is partly transparent only during a short time at the beginning of the interaction. Once the target has reached a relativistic velocity, the radiation pressure in the target frame is lower and electrons remain confined in the target. On such long times, the CEL does not actually stay at the target rear side and ion acceleration becomes more similar to multistage acceleration.

Figure 4 also reveals the quasi-monoenergetic ion distribution during the acceleration process. This is underlined in the different panels of figure 4 presenting the ion energy at the end

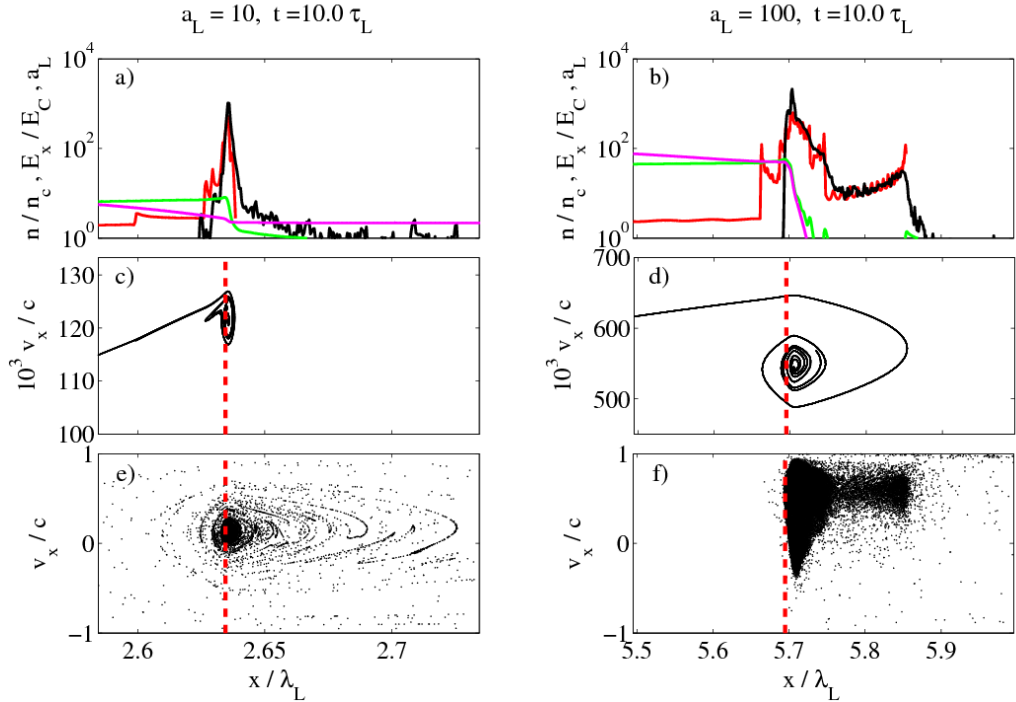


Figure 5. Phase-stable acceleration ($\xi = 1$). Details of the target $10 \tau_L$ after the beginning of the interaction for (a, c, e) $a_0 = 10$ and (b, d, f) $a_0 = 100$. (a, b) The laser field amplitude is shown in magenta, the electrostatic field in green and the ion and electron densities in red and black, respectively. (c, d) Ion distribution in phase space. (e, f) Electron distribution in phase space. See also movies of the whole simulation corresponding to (a, c, e) and (b, d, f), available from stacks.iop.org/NJP/13/123003/mmedia (movies 1 and 2).

of the interaction process (panels 4(e)–(h)), as well as in figure 6, which shows the relative ion energy dispersion as a function of the ion mean energy for $a_0 = 10$ – 100 . Figure 6 also confirms the characteristic dependence of the relative energy dispersion, which is proportional to $\mathcal{E}_i^{-1/2}$ as predicted by equation (11). Equation (11) also predicts that $\Delta\mathcal{E}_i/\mathcal{E}_i$ should scale as $\sqrt{l_e a_0}$, and one could naively expect for a given ion mean energy that $\Delta\mathcal{E}_i/\mathcal{E}_i$ scales as the square root of the laser field amplitude a_0 . Figure 6, however, shows that the dependence on a_0 is stronger. This is because the CEL thickness l_e actually increases with a_0 for a fixed value of $\xi \propto d_0/a_0$.

Let us now discuss the fraction f_i of ions in the monoenergetic peak. A naive estimate can be derived from the semi-microscopic model presented in section 3.1 by considering that only ions initially located in the CEL participate in the phase-stable acceleration so that $f_i \sim 1 - \xi^{-1}$ (see also [26]). This estimate would suggest that only a very small fraction of the target ions participate in the acceleration process. Simulations, however, show quite the contrary: f_i ranges between 0.45 and 0.67 for $a_0 = 10$ – 100 . There are two reasons for such a high number of accelerated ions. (i) While in the model presented in section 3.1 the CEL thickness shrinks to 0 as $\xi \rightarrow 1$, the electron pressure in the CEL actually increases during the compression by the laser pulse and prevents its collapse. As a result, the CEL thickness is much larger than expected in the model and so is the fraction of accelerated ions. (ii) Furthermore, some ions initially located outside of the CEL can still be injected (after

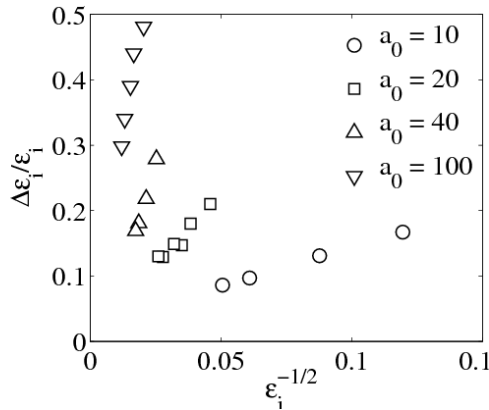


Figure 6. Phase-stable acceleration ($\xi = 1$). Relative energy dispersion during the phase-stable acceleration as a function of the ion mean energy. For $a_0 = 10$ (\circ), $a_0 = 20$ (\square), $a_0 = 40$ (\triangle) and $a_0 = 100$ (∇).

some time) in the CEL and thereafter participate in the phase-stable acceleration. While the creation of the CEL is almost instantaneous (because of electron relativistic velocities, it occurs on a characteristic time $\sim d_0/c \ll 1$), ions react to the strong electrostatic field on a longer time scale of the order of the inverse ion plasma frequency. A self-maintained structure made of both the CEL and ions is formed and it is this structure which is accelerated in a phase-stable way. The correct modeling of this accelerating structure is very challenging as it would require one to describe self-consistently the ion and electron motions. While this has been done for ion acceleration in the HB regime in [24] by developing a quasi-stationary model, this is particularly difficult under current conditions as the quasi-stationary hypothesis does not hold. What is also clearly highlighted in the two movies is that some ions, which are not initially located inside the accelerating structure, can be injected into it after some time. Ions located outside the CEL indeed ‘see’ a constant accelerating field and may actually catch up with the CEL after some time. For nonrelativistic ions, one can easily estimate that only ions initially located at a position $x_{i0} > d_0/2$ can reach the CEL and their fraction f_i cannot exceed 50%. Accounting for relativistic effects allows for a larger fraction of reinjected ions (which increases in time, according to simulations, up to 67% for $a_0 = 100$). Similar features have been reported by Eliasson *et al* [25] using the Vlasov–Maxwell simulations. Considering a thin foil with dimensionless parameter $\xi \sim 1.8$ ($Z n_{i0} = 10$, $d_0 = 0.2 \lambda_L$ and $a_0 = 5$), the authors found that between 75 and 80% of the ions are efficiently accelerated and that relativistic effects help in increasing this fraction.

Finally, we want to point out that, once the laser is turned off, the energy stored in the electrostatic field goes back to electrons, which start quivering around the accelerated ions, thus driving its adiabatic expansion. If the electrostatic energy is of the same order of magnitude as the total ion energy, this can strongly enhance the final ion energy dispersion. To investigate this effect in depth, we have plotted the total energy of ions in the monoenergetic peak and the energy stored in the electrostatic field as a function of time for $a_0 = 10$ –100 in figure 7. For small laser amplitudes $a_0 = 10$ –20 and correspondingly non-relativistic ion energies, a non-negligible fraction of the energy ($\approx 30\%$) is stored in the electrostatic field. As a consequence, the corresponding ion energy spectra (figures 4(i) and (j)) are considerably wider at the end of

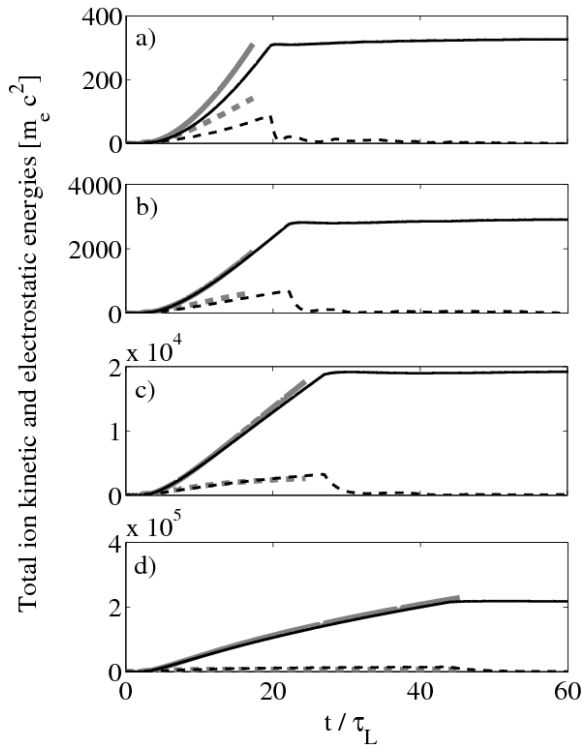


Figure 7. Phase-stable acceleration ($\xi = 1$). Temporal evolution of the total kinetic energy of ions in the monoenergetic peak (solid curves) and the energy stored in the electrostatic field (dashed curves) for (a) $a_0 = 10$, (b) $a_0 = 20$, (c) $a_0 = 40$ and (d) $a_0 = 100$. Gray lines show theoretical predictions from section 3.1.

the simulation. In contrast and as predicted in section 3.1, this effect is negligible for sufficiently large ion energies. For $a_0 = 40$ – 100 , most of the energy is stored in the accelerated ion bunch and non-enhanced ion energy dispersion is observed (figures 4(k) and (l)).

In addition, we note that this effect can also be mitigated at low ion energy by using a more sophisticated laser pulse temporal profile, e.g. by considering Gaussian or hyper-Gaussian pulses. Figure 8 shows the ion energy spectra obtained using a sixth-order hyper-Gaussian or Gaussian laser pulse with similar maximum field amplitude $a_0 = 10$, fluence and full-width at half-maximum. The enhanced energy dispersion due to the long-time behavior of electrons is strongly mitigated as the pulse is slowly turned off.

4.3. Ion acceleration in the multistage regime

PIC simulations in the regime of multistage acceleration ($\xi \gg 1$) are now discussed. Figure 9 shows the time resolved ion energy spectra extracted from simulations with $\xi = 4$ and different laser field amplitudes ($a_0 = 10$ – 100). In these simulations, the laser temporal envelope $a_L(t)$ is constant over a duration corresponding to $20 t_0$ (we recall that $t_0 = d_0/v_{p0}$ is the characteristic duration of an acceleration stage). Theoretical predictions from the model developed in section 3.2 are superimposed on the numerical results. Rather good agreement on the minimum and maximum ion energies as a function of time is found between theory and simulations: our

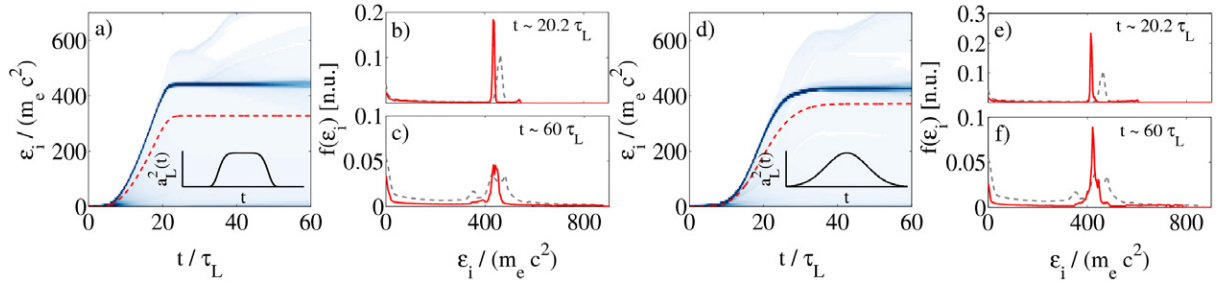


Figure 8. Phase-stable acceleration ($\xi = 1$). The same as figure 4 for $a_0 = 10$ and two different laser intensity profiles: (a–c) for a sixth-order hyper-Gaussian profile and (d–f) for a Gaussian profile. Red dashed lines in panels (a) and (d) show theoretical predictions from the light-sail model (solutions of equation (2)). Gray dashed lines in panels (b, c, e, f) show the energy spectra obtained using a rectangular laser temporal envelope $a_L(t)$ as shown in figure 4 (e, i).

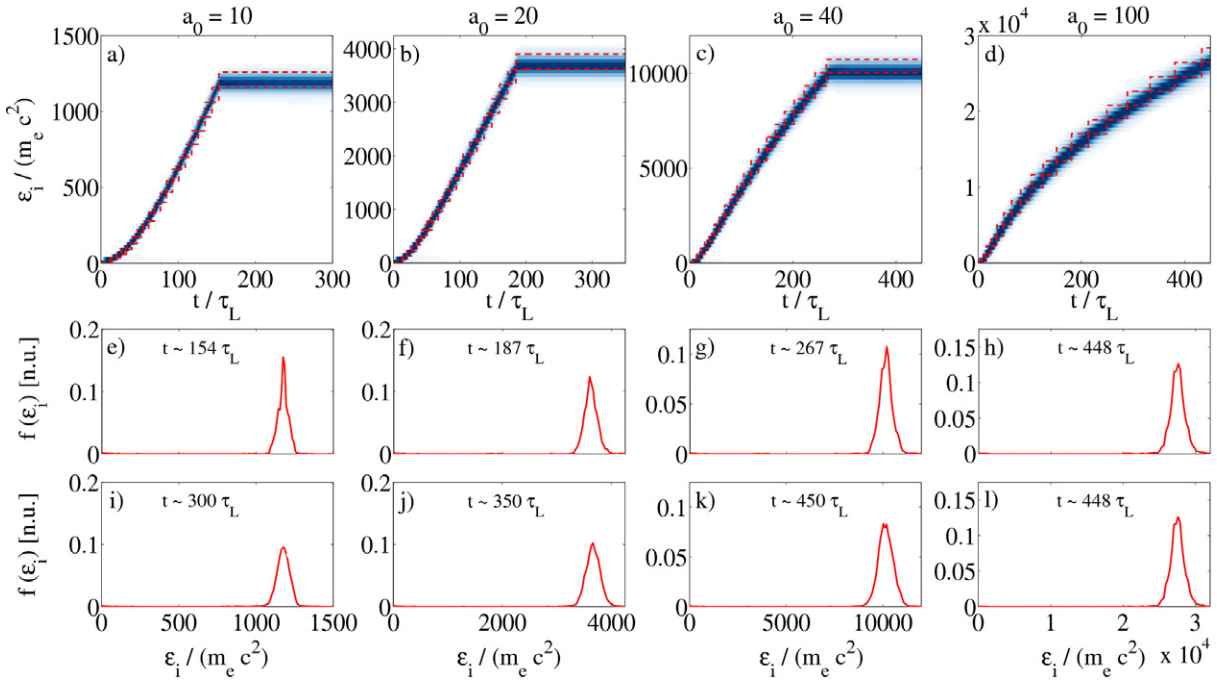


Figure 9. Multistage acceleration ($\xi = 4$). (a–d) Time-resolved ion energy spectra. (e–h) Snapshot of the energy spectrum at the end of the laser-target interaction. (i–l) Snapshot of the energy spectrum at the end of the simulation. The laser field amplitude is (a, e, i) $a_0 = 10$, (b, f, j) $a_0 = 20$, (c, g, k) $a_0 = 40$ and (d, h, l) $a_0 = 100$. Red dashed lines in panels (a–d) show theoretical predictions from the iterative model (section 3.2).

model allows us to correctly predict both the ion mean energy and energy dispersion. For the cases with $a_0 = 40$ and $a_0 = 100$, ions quickly reach relativistic energies and the dilation in the laboratory frame of the characteristic stage duration becomes obvious. Also, the duration of the laser–target interaction (and therefore of the acceleration process) increases as the foil reaches larger velocities (figure 9).

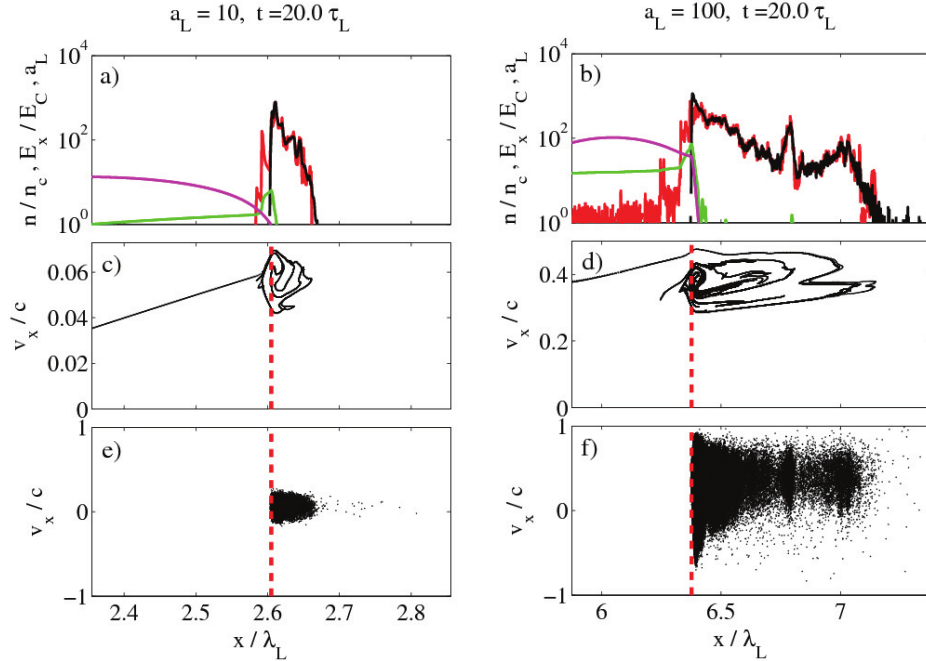


Figure 10. Multistage regime ($\xi = 4$). Details of the target $20 \tau_L$ after the beginning of the interaction for (a, c, e) $a_0 = 10$ and (b, d, f) $a_0 = 100$. (a, b) The laser field amplitude is shown in magenta, the electrostatic field in green and the ion and electron densities in red and black, respectively. (c, d) Ion distribution in phase space. (e, f) Electron distribution in phase space. See also movies of the whole simulation corresponding to (a, c, e) and (b, d, f), available from stacks.iop.org/NJP/13/123003/mmedia (movies 3 and 4).

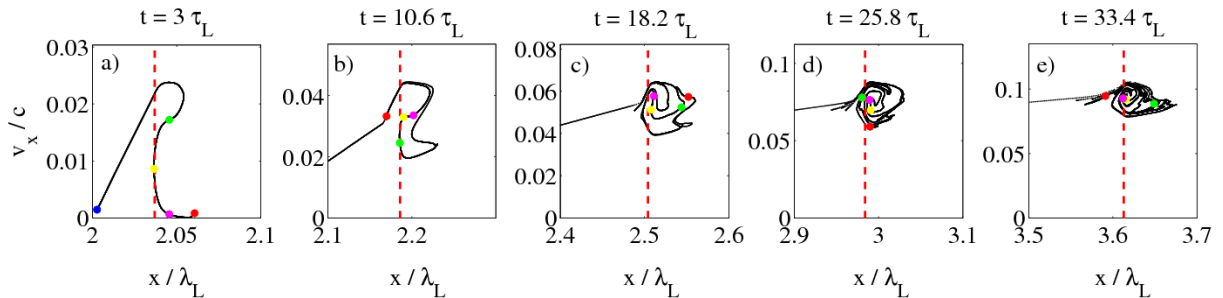


Figure 11. Multistage regime ($\xi = 4$). Ion phase space at different times after the beginning of interaction: (a) $3 \tau_L$, (b) $10.6 \tau_L$, (c) $18.2 \tau_L$, (d) $25.8 \tau_L$ and (e) $33.4 \tau_L$. Each time corresponds to a different acceleration stage. In this simulation, $a_0 = 10$ and $\xi = 4.0$. The colored dots follow test ions during the acceleration process. The vertical dashed line shows the position of the laser piston (position of the maximum electrostatic field).

Additional details of the target structure as well as the ion and electron phase-space distributions during the acceleration process are given in figures 10 and 11 and in the corresponding movies. The transition between successive acceleration stages is clearly visible in the movies. For the case $a_0 = 10$ for instance, the first HB stage terminates at $t \simeq 16 \tau_L$. As ions

are reflected again and again by the laser piston, their distribution in phase space becomes more and more complex in contrast to what was observed during phase-stable acceleration (compare, for instance, figures 10(c) and (d) and figures 5(c) and (d)).

Furthermore, the ion energy spectra at the end of the simulations (figures 9(i)–(l)) are quite similar to those obtained at the end of the laser–target interaction (figures 9(e)–(h)). In contrast to phase-stable acceleration, the ion energy distribution here is not sensitive to the late-time behavior of the electrons. This is due to the small fraction of laser energy which is stored in the electrostatic field at $\xi \gg 1$.

This excellent control of the ion beam spectrum as well as the large fraction of accelerated ions (f_i exceeds 90% in these simulations) makes this regime of acceleration particularly attractive for high-quality ion beam generation. Similarly, in [25], the authors report a fraction $f_i \sim 95\%$ of accelerated ions for a foil with a dimensionless parameter $\xi \sim 3.6$ ($Z n_{i0} = 10$, $d_0 = 0.4 \lambda_L$ and $a_0 = 5$). Numerical simulations also suggest that RPA proceeds in the multistage regime as soon as $\xi \gtrsim 2$, which makes this robust mechanism more likely to be observed in experiments than phase-stable acceleration.

Finally, as RPA in the multistage regime follows from successive HB of the target, one may suggest an additional source of energy dispersion for large laser field amplitudes and/or rather thick targets. Recent studies have indeed underlined the non-stationary behavior of the laser piston at high laser intensities giving rise to the so-called piston oscillations [24]. This phenomenon implies large-amplitude (typically $\simeq 30\%$) oscillations of the maximum electrostatic field in the laser piston, leading to an enhanced energy dispersion of ions reflected during the HB process. While the origin of these oscillations is not yet fully understood, some of their characteristic features are known: (i) their characteristic period is of the order of the inverse ion plasma frequency ($\omega_{pi} = \sqrt{Z^2 n_{i0}/m_i}$ in our normalized units), (ii) they appear after a characteristic time t_s , which is shorter for larger laser field amplitudes and/or target densities. For instance, PIC simulations of HB of a thick carbon foil with ion density $n_{i0} = 25$ by a CP laser pulse with $a_0 = 40$ indicate that oscillations in the electrostatic field with a characteristic period $\simeq 1.4 \tau_L$ and $\simeq 35\%$ amplitude with respect to the maximum field strength occur after a time $t_s \simeq 5 \tau_L$. Increasing the laser field amplitude to $a_0 = 100$ does not change the relative amplitude of the oscillations or their period but shortens the characteristic time of their appearance to $t_s \simeq 3.7 \tau_L$.

One could therefore fear that these piston oscillations widen the energy spectrum during the multistage acceleration. Clearly, this is not the case in the simulations presented in figure 9, where the energy dispersion is well described by our multistage model (which does not account for the piston oscillations). However, for these simulations, the characteristic duration of an acceleration stage $t_0 \sim d_0/v_{p0} \simeq 6 \tau_L$ is rather short and the piston oscillations have scarcely the time to develop. Therefore, we have performed a simulation with a thicker target ($\xi = 10$ and $a_0 = 40$). The results of this simulation are presented in figure 12. During the first acceleration stage, for $t = 0$ – $16 \tau_L$, oscillations in the maximum electrostatic field are clearly visible after a time $t \simeq 5 \tau_L$ (figure 12(b)) and result in a rather complex ion phase-space distribution (figure 12(c) as compared to figure 11(a)). Nevertheless, these regular oscillations disappear at the end of the first stage ($t > 16 \tau_L$), which we attribute to the already perturbed target configuration in the second acceleration stage. There are still some large variations in the maximum value of the electrostatic field, but these variations are generic to all realistic simulations we have performed in the multistage regime. They follow more from the global ion dynamics in the target than from the piston oscillations themselves. Hence, these results suggest

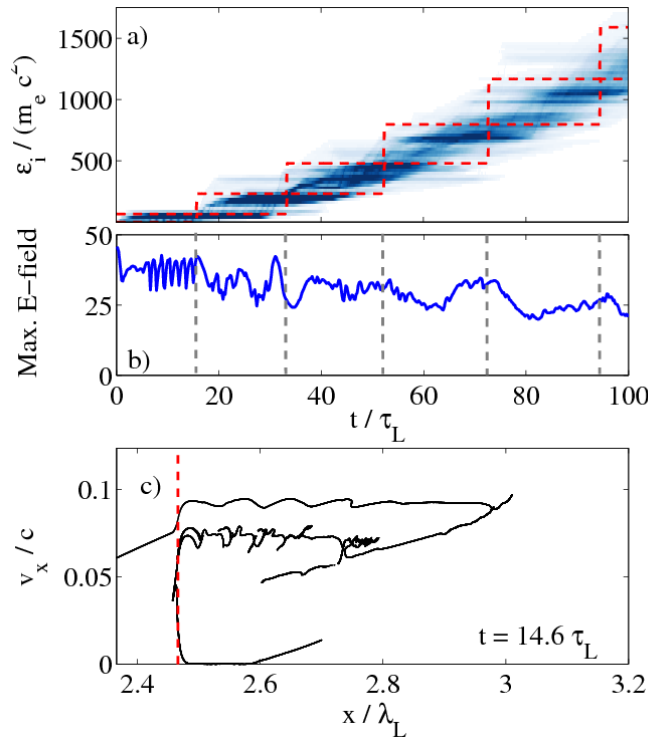


Figure 12. Multistage regime ($\xi = 4$). (a) Time-resolved ion energy spectra. The dashed lines show theoretical prediction from the multistage model. (b) Temporal evolution of the maximum electrostatic field. Vertical gray lines indicate the end of the different acceleration stages as predicted from the multistage model. (c) Ion phase space $14.6\tau_L$ after the beginning of the interaction. The vertical red line shows the position of the laser piston (where the electrostatic field is maximum).

that the so-called piston oscillations are not a concern for the control of ion energy distributions during RPA in thin foils.

5. Conclusion

A detailed study of ion energy dispersion in RPA ion beams is presented using both analytical modeling and 1D3V PIC simulations. The description proposed here allows for a greater insight into the details of RPA of thin foils than the standard macroscopic light-sail model. In particular, our description provides us with necessary conditions for quasi-monoenergetic ion beam generation.

Two RPA regimes are identified depending on the dimensionless parameter ξ which determines, for a given target density and laser field amplitude, the target thickness. For both regimes, the models we have developed allow us to recover the ion energy temporal evolution obtained by considering efficient momentum transfer from the laser photons to the target ions (the usual light-sail model). By accounting for the target structure during the acceleration process, we can even retrieve the ion energy dispersion.

For $\xi \sim 1$ (thin targets), the strong radiation pressure pushes all electrons to the target rear side. A large electrostatic field is built up in the whole target and ions are continuously accelerated. RPA then proceeds in the phase-stable regime introduced in [9]. Two sources of energy dispersion have been identified in this regime: the electric field inhomogeneity in the accelerating structure, and the adiabatic foil expansion due to the late-time electron behavior. This later process is important mainly for low-energy ions and its effect can be mitigated by using smooth temporal laser profiles. We also recall that predicting more accurately the energy dispersion in this regime would require us to compute the thickness of the CEL, which cannot be done using the present model.

For $\xi \gtrsim 2$ (thicker targets), the radiation pressure is not strong enough to push electrons to the target rear side. Instead, the electrostatic field is confined to a very thin region (compared to the target thickness). It forms the so-called laser piston. Ion acceleration is not continuous anymore and it proceeds in a multistage regime as originally discussed in [6, 7] and for which we have developed a simple but sound model. Ion energy dispersion in this regime is mainly determined by the number of acceleration stages. Small-energy dispersion can thus be achieved by using long enough laser pulses.

Furthermore, it is worth underlining that, in simulations, the two acceleration regimes can be distinguished when considering the ion distribution in phase space (x, v_x) . Indeed, while the ion phase space has a rather simple, spiral-like shape in the phase-stable acceleration, it is much more complex in the multistage regime due to the successive HB processes.

Finally, this work suggests that using moderately intense (and long) laser pulses is preferable for monoenergetic ion beam generation. The lower limit on the laser intensity actually follows from the need to accelerate the ions to the desired energy before the target escapes from the laser focal volume. As for the optimal target thickness, the thinner the target, the higher the ion energies one can reach. However, maintaining the target integrity in the regime $\xi \rightarrow 1$ might be experimentally difficult. Any non-uniformity in the laser intensity profile may lead to the removal of electrons and the resulting Coulomb explosion of the target. Also, Rayleigh–Taylor-like instabilities, which have been observed in 2D simulations [7], may be more detrimental for very thin targets. Since simulations suggest that RPA occurs in the multistage regime as soon as $\xi \gtrsim 2$, phase-stable acceleration may thus be difficult to achieve in experiments. We therefore expect multistage acceleration to be the practically relevant acceleration mechanism.

Acknowledgments

We are grateful to E d’Humières and Y Sentoku for providing us with the PICLS code.

References

- [1] Wilks S C, Langdon A B, Cowan T E, Roth M, Singh M, Hatchett S, Key M H, Pennington D, MacKinnon A and Snavely R A 2001 *Phys. Plasmas* **8** 542
- [2] Mora P 2003 *Phys. Rev. Lett.* **90** 185002
- [3] Marx G 1966 *Nature* **211** 22
- [4] Esirkepov T, Borghesi M, Bulanov S V, Mourou G and Tajima T 2004 *Phys. Rev. Lett.* **92** 175003
- [5] Macchi A, Cattani F, Liseykina T V and Cornolti F 2005 *Phys. Rev. Lett.* **94** 165003
- [6] Zhang X, Shen B, Li X, Jin Z and Wang F 2007 *Phys. Plasmas* **14** 073101
- [7] Klimo O, Psikal J, Limpouch J and Tikhonchuk V T 2008 *Phys. Rev. ST Accel. Beams* **11** 031301

- [8] Robinson A P L, Zepf M, Kar S, Evans R G and Bellei C 2008 *New J. Phys.* **10** 013021
- [9] Yan X Q, Lin C, Sheng Z M, Guo Z Y, Liu B C, Lu Y R, Fang J X and Chen J E 2008 *Phys. Rev. Lett.* **100** 135003
- [10] Rykovanov S G, Schreiber J, Meyer-ter-Vehn J, Bellei C, Henig A, Wu H C and Geissler M 2008 *New J. Phys.* **10** 113005
- [11] Tripathi V K, Liu C S, Shao X, Eliasson B and Sagdeev R Z 2009 *Plasma Phys. Control. Fusion* **51** 024014
- [12] Macchi A, Veghini S and Pegoraro F 2009 *Phys. Rev. Lett.* **103** 085003
- [13] Qiao B, Zepf M, Borghesi M and Geissler M 2009 *Phys. Rev. Lett.* **102** 145002
- [14] Pegoraro F and Bulanov S V 2007 *Phys. Rev. Lett.* **99** 065002
- [15] Bulanov S V, Echkina E Yu, Esirkepov T Zh, Inovenkov I N, Kando M, Pegoraro F and Korn G 2010 *Phys. Rev. Lett.* **104** 135003
- [16] Chen M, Pukhov A, Yu T P and Sheng Z M 2009 *Phys. Rev. Lett.* **103** 024801
- [17] Henig A *et al* 2009 *Phys. Rev. Lett.* **103** 245003
- [18] Liechtenstein V Kh, Ivkhova T M, Olshanski E D, Repnow R, Steier P, Kutschera W, Wallner A and Von Hahn A 2006 *Nucl. Instrum. Methods Phys. Res. A* **561** 120
- [19] Tajima T, Habs D and Yan X Q 2009 *Rev. Accel. Sci. Tech.* **2** 201
- [20] Kulagin V V, Cherepenin V A, Hur M S and Suk H 2007 *Phys. Rev. Lett.* **99** 124801
- [21] Grech M, Skupin S, Nuter R, Gremillet L and Lefebvre E 2009 *New J. Phys.* **11** 093035
- [22] Grech M, Skupin S, Nuter R, Gremillet L and Lefebvre E 2010 *Nucl. Instrum. Methods Phys. Res. A* **620** 63
- [23] Naumova N, Schlegel T, Tikhonchuk V T, Labaune C, Sokolov I V and Mourou G 2009 *Phys. Rev. Lett.* **102** 025002
- [24] Schlegel T, Naumova N, Tikhonchuk V T, Labaune C, Sokolov I V and Mourou G 2009 *Phys. Plasmas* **16** 083103
- [25] Eliasson B, Chuan S L, Shao X, Sagdeev R Z and Shukla P K 2009 *New J. Phys.* **11** 073006
- [26] Macchi A, Veghini S, Liseykina T V and Pegoraro F 2010 *New J. Phys.* **12** 045013
- [27] Sentoku Y and Kemp A 2008 *J. Comput. Phys.* **227** 6846